Journal of Japan Association for Earthquake Engineering, Vol. 25, No. 13, 2025
[Technical Paper (Translated Paper)]

COSEISMIC FAILURE ANALYSIS OF EMBANKMENTS USING 3D EARTHQUAKE RESPONSE AND CRACK PROPAGATION ANALYSIS METHOD

Taiki SHIMBO[1], Chia KANADA[2], Tomoki KAWAMURA[3] and Yutaka FUKUMOTO[4]

[1] Dr. Eng., Associate Professor, Department of Civil Engineering, National Institute of Technology, Ishikawa College, Ishikawa, Japan, shimbo@ishikawa-nct.ac.jp
[2] Alumni, National Institute of Technology, Ishikawa College, Ishikawa, Japan
[3] Ph. D., Godai KAIHATSU Corp, Ishikawa, Japan, kawamura@godai.co.jp
[4] Dr. Agr., Associate Professor, Faculty of Environmental, Life, Natural Science and Technology, Okayama University, Okayama, Japan, yutakafukumoto@okayama-u.ac.jp

ABSTRACT: The types of embankment damage during earthquakes are crest or slope tension cracking and circular sliding. However, it remains unclear which damage occurs during which earthquake. In a previous study, we conducted a crack propagation analysis using Peridynamics (PD) to examine various embankment damage types. The results showed that the type of damage varies with the maximum acceleration and frequency. However, the analysis was limited to two dimensions. Therefore, in this study, a three-dimensional seismic response PD was developed and compared with the two-dimensional PD to demonstrate the validity of the code. We also investigated the influence of the maximum acceleration and frequency on the failure modes.

Keywords: *Embankment, Crack propagation analysis, 3D analysis*

1. INTRODUCTION

In Japan, Level 2 seismic performance evaluation of embankments is currently conducted using the Newmark method[1)], a rigid-body-based analysis approach that assumes circular slip surfaces to calculate the settlement of sliding soil masses. However, cases where longitudinal tensile cracks form at the crest or slope of embankments during earthquakes, as well as cracks propagating from the crest to the base of embankments and separation-type failures caused by cracking due to liquefaction within embankments during seismic events have been reported[2)–7)]. Moreover, cracks induced by earthquakes in natural slopes that subsequently trigger landslides during rainfall have also been detected[8)], suggesting the potential for similar damage to occur in embankments. Therefore, to properly evaluate the seismic performance of embankments, including both tensile cracking and sliding failures, an analysis method that can simultaneously consider the three-dimensional (3D) development of such failures during seismic loading is required. However, the conditions under which different types of failures occur during earthquakes remain unclear.

Shimbo[9)] proposed a method for calculating the residual displacement of sliding soil masses by incorporating existing cracks (i.e., sliding surface) using the extended finite element method (X-FEM), which can account for ground deformation characteristics and seismic response acceleration. Ikeda et al.[6)] proposed an analysis approach using X-FEM that considers both tensile cracking and shear failure in embankments during earthquakes. Harada et al.[5)], using X-FEM on embankments built over liquefiable ground, demonstrated that the location of tensile crack initiation varies with the embankment height and input wave frequency. Furthermore, the present authors previously proposed and verified[10)–14)] a numerical analysis method called Peridynamics (PD) that could simulate spontaneous crack initiation and propagation and applied PD to analyze embankments formed with compacted clay[12), 13)] by incorporating their fracture toughness values[15)]. These studies suggested that a higher-frequency input tends to induce cracks from the slope, whereas a lower-frequency input is more likely to result in sliding failure. However, these analyses were limited to two dimensions and did not capture 3D features such as longitudinal cracking.

In explicit crack representation methods, such as the double node method or X-FEM, cracks must be defined as curved surfaces in 3D space. This introduces difficulties in geometric processing, such as the initialization of crack surfaces, propagation from arbitrary locations, intersection between crack surfaces, and crack branching behavior. In contrast, PD models the interaction between particles using spring-like bonds within a specified influence domain centered on each particle. Cracks are expressed by breaking these bonds on the basis of fracture toughness criteria. Therefore, PD can represent crack initiation, propagation from any point on a curved surface, intersections, and branching behavior in 3D without requiring geometric operations.

The present authors previously proposed a coupled analysis method that integrated 3D PD with the discrete element method and conducted contact fracture simulations of spherical bodies formed from cohesive soil materials[16)]. However, a 3D PD formulation that incorporates seismic response has not yet been developed. Accordingly, this study presents a foundational investigation where a 3D seismic response PD model incorporating Rayleigh damping in a linearly isotropic elastic body is developed. To verify the proposed analysis code, failure modes obtained from two-dimensional (2D) PD seismic analyses are compared. Furthermore, this study reports the effects of input wave frequency and peak acceleration on the failure behavior of embankments with 3D geometries.

2. OVERVIEW OF THE ANALYSIS AND MODELING

2.1 Equations of motion and analysis framework

PD, proposed by Silling[17)], is a nonlocal formulation of continuum mechanics introduced to address displacement discontinuity problems. The discretized form of the ordinary state-based PD, incorporating seismic waves (input acceleration) and Rayleigh damping, is given by the following equation[10)]:

$$\begin{aligned}\rho\ddot{\mathbf{u}}(\mathbf{x}_i,t)+\rho\alpha\dot{\mathbf{u}}(\mathbf{x}_i,t)&=\sum_{j=1}^{N_H}\left\{\underline{\mathbf{T}}(\mathbf{x}_i,t)-\underline{\mathbf{T}}(\mathbf{x}_j,t)\right\}V_j\\&+\beta\frac{d}{dt}\left[\sum_{j=1}^{N_H}\left\{\underline{\mathbf{T}}(\mathbf{x}_i,t)-\underline{\mathbf{T}}(\mathbf{x}_j,t)\right\}V_j\right]+\rho\mathbf{g}(\mathbf{x}_i)-\rho\ddot{\mathbf{u}}_g\end{aligned}\tag{1}$$

Here, ρ denotes density; α and β are the Rayleigh damping parameters corresponding to mass-proportional and stiffness-proportional damping, respectively; t represents the analysis time; N_{H} is the number of particles within the horizon; x_i is the position vector of the central particle; j denotes neighboring particles (excluding i) within the horizon; u is the relative displacement vector between particles; V_j is the volume associated with particle j; $\mathbf{g}(x_i)$ denotes the gravitational acceleration at x_i; $\ddot{\mathbf{u}}_g$ represents the input acceleration; and $\underline{\mathbf{T}}$ is the force density vector, corresponding to the constitutive model. The constitutive relation assumes a linearly isotropic elastic body, following the formulation of Madenci and Oterkus[18]. Let y denote the deformed position and δ the radius of the horizon, then the force density vector $\underline{\mathbf{T}}$ is given by the following equation. The related quantities are defined as follows: stretch is given in Eq. (3); volumetric stretch in Eq. (4); the influence function in Eq. (5); and the physical quantities and 3D analysis parameters in Eq. (6). Here, κ and μ denote the bulk and shear moduli, respectively.

$$\underline{\mathbf{T}}(\mathbf{x}_i,t)=\frac{1}{2}A\frac{\mathbf{y}_j-\mathbf{y}_i}{\left|\mathbf{y}_j-\mathbf{y}_i\right|},A=4\left(\delta b s_{ij}+ad\omega_{ij}\Lambda_{ij}\theta_i\right),\Lambda_{ij}=\frac{\mathbf{y}_j-\mathbf{y}_i}{\left|\mathbf{y}_j-\mathbf{y}_i\right|}\cdot\frac{\mathbf{x}_j-\mathbf{x}_i}{\left|\mathbf{x}_j-\mathbf{x}_i\right|} \tag{2}$$

$$s_{ij}=\frac{\left|\mathbf{y}_j-\mathbf{y}_i\right|-\left|\mathbf{x}_j-\mathbf{x}_i\right|}{\left|\mathbf{x}_j-\mathbf{x}_i\right|} \tag{3}$$

$$\theta_i=d\delta\sum_{j=1}^{N_H}s_{ij}\Lambda_{ij}V_j \tag{4}$$

$$\omega_{ij}=\frac{\delta}{\left|\mathbf{x}_j-\mathbf{x}_i\right|} \tag{5}$$

$$a=\frac{1}{2}\left(\kappa-\frac{5}{3}\mu\right),b=\frac{15\mu}{2\pi h\delta^5},d=\frac{9}{4\pi\delta^4} \tag{6}$$

The numerical integration of Eq. (1) was performed using the velocity Verlet method[19], which is commonly employed in molecular dynamics. Specifically, the velocity and displacement at the next time step are computed as follows:

$$\begin{aligned}\mathbf{u}(\mathbf{x}_i,t+\Delta t)&=\mathbf{u}(\mathbf{x}_i,t)+\dot{\mathbf{u}}(\mathbf{x}_i,t)\Delta t+\frac{1}{2}\ddot{\mathbf{u}}(\mathbf{x}_i,t)\Delta t^2\\ \dot{\mathbf{u}}(\mathbf{x}_i,t+\Delta t)&=\dot{\mathbf{u}}(\mathbf{x}_i,t)+\frac{1}{2}\left\{\ddot{\mathbf{u}}(\mathbf{x}_i,t)+\ddot{\mathbf{u}}(\mathbf{x}_i,t+\Delta t)\right\}\Delta t\end{aligned} \tag{7}$$

Here, Δt is the time increment, and $\ddot{\mathbf{u}}(\mathbf{x}_i,t+\Delta t)$ is computed from Eq. (1). Regarding the contact conditions, short-range forces were applied to prevent particle interpenetration, whereas frictional effects were omitted for simplicity. To address the integration accuracy degradation near boundaries, the domain correction method proposed by Madenci and Oterkus[18] was adopted.

To represent the sliding failure in this study, gravity loading analysis was performed without displacement reset. The gravity analysis was continued until the acceleration response due to self-weight became sufficiently small, after which the seismic input was applied. If a displacement reset was applied, then the driving force due to the self-weight disappeared, preventing subsequent sliding failure. Thus, no displacement reset was conducted, and the residual settlement from the gravity analysis was carried over into the seismic response analysis.

In this first study, displacement-fixed boundary conditions were imposed on the bottom of the model. The input acceleration was applied horizontally to the embankment, as described later, using E + F waves. The incorporation of viscous boundary conditions is to be addressed in future work.

2.2 Analysis conditions

In this study, seismic failure analyses (i.e., seismic response and crack propagation analyses) were conducted on an embankment composed of a homogeneous material. The material properties of the embankment were obtained from unconfined compression tests using blue clay at a moisture content of w = 18% and a compaction ratio of 90%[15]. The measured properties include a density of 1,761 kg/m³,

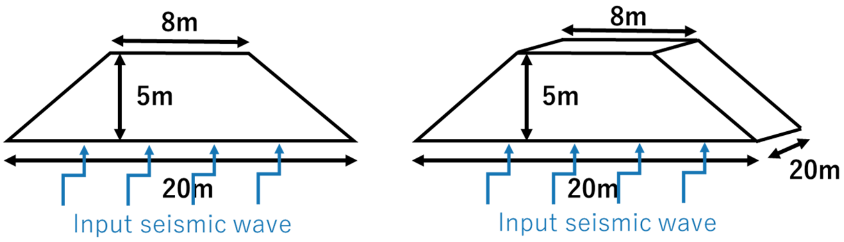

(a) Overview of the 2D model (b) Overview of the 3D model

Fig. 1 Conceptual diagrams of the analysis models

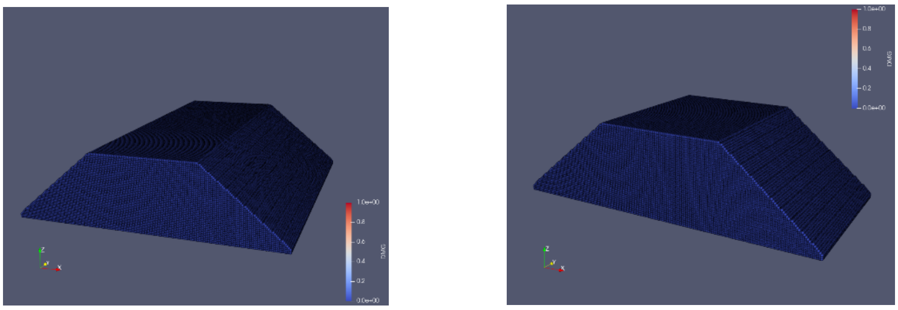

(a) View of the entire model (b) Central cross-section at a 10 m depth

Fig. 2 3D analysis model

a Young's modulus of 8.5 MPa, a Poisson's ratio of 1/4, an unconfined compressive strength of 107 kPa, and an undrained shear strength C_u of 53.8 kPa (based on the method $\phi_u = 0°$). The fracture toughness was defined as $K_{IIC} = 6.204$ kPa·m$^{0.5}$.

The fracture toughness values K_{IC} and K_{IIC} represent the stress intensity factors at the onset of crack propagation. The subscript I denotes Mode I (tensile fracture), II denotes Mode II (shear fracture), and C denotes a critical (fracture) state. The K_{IIC} value used in this study was determined as follows. Uniaxial compression tests were performed on cylindrical specimens with initial cracks (length $2a$, inclined at 45°) under varying moisture contents w. The stress σ at the onset of crack propagation was used to compute the stress intensity factor $K_{IIC} = \sigma / 2\sqrt{\pi a}$ 15). An approximate linear relationship without cross-sectional correction in computing the stress intensity factor, $K_{IIC} = -0.376w + 12.972$, was derived and used for this study. These tests were conducted under conditions where $K_{IIC} = K_{IC}$. Thus, the same value can reasonably be applied to tensile failure as well.

Rayleigh damping parameters were set to achieve a damping ratio $h = 5\%$ over all frequencies, with a seismic duration $D = 30$ s, time increment $T_i = 0.01$ s, minimum angular frequency $\omega_{min} = 2\pi/D$, and maximum angular frequency $\omega_{max} = \pi/T_i$. On this basis, the Rayleigh coefficients were computed as $\alpha = 0.02093$ and $\beta = 0.00032$ using the following equations:

$$\alpha = \frac{2\omega_{max}\omega_{min}}{\omega_{max}+\omega_{min}} h,\ \beta = \frac{2h}{\omega_{max}+\omega_{min}} \tag{8}$$

An overview of the analysis models is shown in Fig. 1. Both the 2D and 3D models had an embankment height of 5 m, a crest width of 8 m, and a base width of 20 m. The 2D analysis was performed under plane strain conditions, whereas the 3D model had a depth of 20 m. In the 3D analysis, to prevent displacement in the depth direction, nonfracturing walls were placed at the front and back of the model, allowing only vertical displacement. The allowance for vertical displacement was necessary to avoid artificial stress concentrations at the embankment-wall boundary during the seismic response analysis given the mismatch in settlement after the gravity loading stage.

The first natural frequency of a horizontally layered ground composed of this material, estimated using the quarter-wavelength rule, is 2.197 Hz. In the PD model, the horizon size δ was set to four times the particle spacing for the 2D analysis and three times for the 3D analysis. The particles were placed in a uniform grid in the x, y, and z directions. The number of particles was 116,524 for the 2D model (with a spacing of 0.025 m) and 1,592,792 for the 3D model (with a spacing of 0.1 m). The constructed 3D model is illustrated in Fig. 2, where Fig. 2(a) shows the entire model and Fig. 2(b) shows a cross-section at the model center. The time increment Δt was set to 10^{-3} s for the gravity loading analysis and 10^{-4} s for the seismic response analysis. The 3D analysis was performed using a Fujitsu supercomputer PRIMEHPC FX1000 and a Fujitsu PRIMERGY GX2570 server (Wisteria/BDEC-01) at the Information Technology Center of the University of Tokyo.

Figure 3 shows an example of the synthetic seismic waveform used in the analysis (maximum acceleration 320 Gal [cm/s²], frequency 1 Hz). The waveform was generated by multiplying a sinusoidal function by an amplitude envelope based on Noda et al.[20] with an equivalent hypocentral distance of 10 km and a magnitude of 7 as parameters. Analyses were conducted while varying the frequency and peak acceleration of the sinusoid. In this study, two cases were examined:

Case (1): Peak acceleration fixed at 320 Gal, with frequencies ranging from 1 to 5 Hz in 1 Hz increments.
Case (2): Frequency fixed at 1 Hz, with peak accelerations ranging from 300 to 400 Gal in 20 Gal increments.

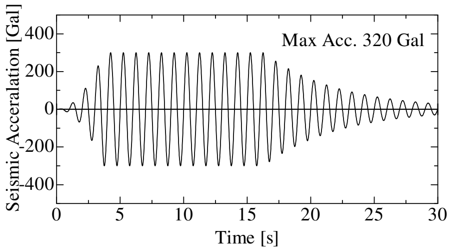

Fig. 3 Synthetic seismic waveform (peak acceleration: 320 Gal; frequency: 1 Hz)

The analysis procedure was as follows. Gravity loading analysis was first performed for 15 s on both the 2D and 3D models. Thereafter, seismic response and crack propagation analyses were conducted by inputting the synthetic seismic waveform at the model base. Crack propagation was represented by breaking bonds between particles when the stretch value, calculated from Eq. (3), exceeded the critical stretch S_{cr}. The critical stretch was derived from the fracture energy release rate G_{c} using the following equation[18]:

$$S_{cr} = \sqrt{\frac{G_c}{\left(3\mu + \left(\frac{3}{4}\right)^4 \left(\kappa - \frac{5}{3}\mu\right)\right)\delta}} \tag{9}$$

The fracture energy G_{c} was calculated from K_{IIC} using the following equation:

$$G_c = \frac{{K_{\mathrm{IIC}}}^2}{E} \tag{10}$$

Damage was quantified as the ratio of broken bonds to the total number of particles within the horizon. For example, a damage value of 0.5 indicated that half the bonds within the horizon were broken. A value of 1 indicated that a particle was completely disconnected and floating. Damage was computed using the following expression[18]:

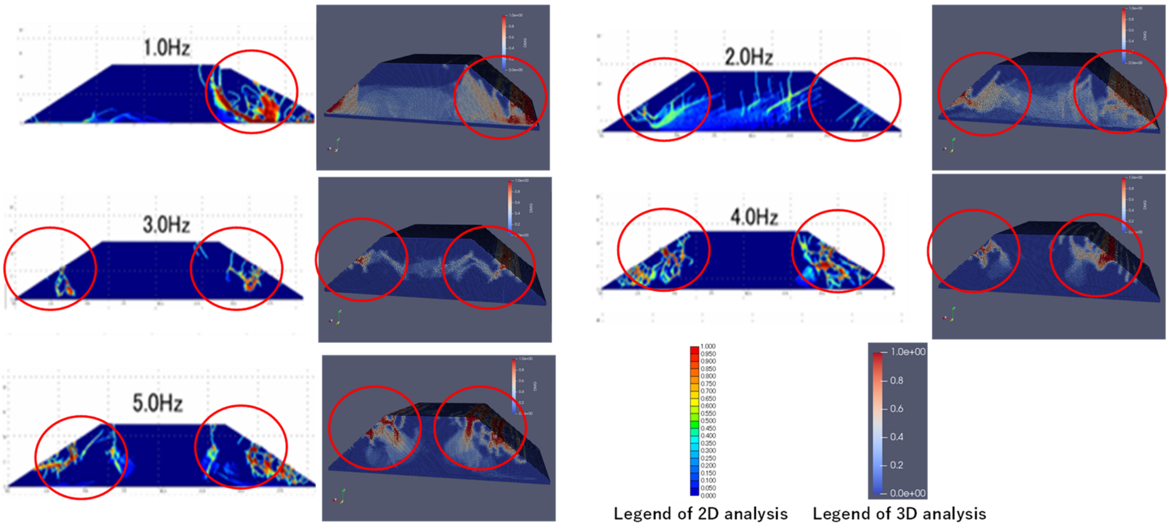

Fig. 4 Damage distribution comparison between the 2D and 3D analyses (central cross-section)

$$\varphi(\mathbf{x},t)=1-\frac{\int_H \mu(\mathbf{x}'-\mathbf{x},t)\,dV}{\int_H dV},\quad \mu(\mathbf{x}'-\mathbf{x},t)=\begin{cases}1 & S<S_c\\ 0 & otherwise\end{cases} \tag{11}$$

3. ANALYSIS RESULTS

3.1 Comparison of failure modes between 2D and 3D analyses (Case (1))

The validity of the developed analysis code was examined by comparing the failure modes obtained from the 2D analysis and those from the central cross-section of the 3D analysis, as shown in Fig. 4. Notably, Fig. 4 shows the state after a crack has formed and the fracture has progressed to some extent. In the figure, red indicates a damage value of 1, and blue indicates a damage value of 0. The legends used in the 3D analysis are consistent throughout the following sections.

As shown in Fig. 4, both the 2D and 3D analyses exhibited sliding failure near the right-side slope at 1 Hz. For frequencies of 2 Hz or higher, the failure progressed after crack formation on the slope. Furthermore, as the frequency increased, the damage tended to concentrate from the mid-slope to the slope shoulder. This trend was consistent between the 2D and 3D analyses. These results indicate that the failure mode obtained in the central section, which approximates a plane strain condition, qualitatively matches that of the 2D analysis, validating the analysis code. However, failure modes in sections other than the central one should be validated in future work through comparison with model tests.

3.2 Analysis results for Case (1)

This section presents the results for Case (1), where the frequency of the sinusoidal wave input was varied. Fig. 5 shows the results for the 1 Hz case. The time indicated in the figure refers to the shaking time after the self-weight analysis. “Entire” refers to the entire model, whereas 5, 10, and 15 m refer to the cross-section locations. At 4.0 s after the self-weight analysis, damage was observed on both slopes (green circle at 5 m, 4.0 s). At 4.2 s, the damage became particularly significant at the toe of the right-side embankment, leading to crack formation. The damage region extended in an arc toward the embankment crest (yellow arrow and green circle at 5 m, 4.2 s). At 4.4 s, a small arc-shaped damage region formed, indicating sliding failure (yellow arrow at 5 m, 4.4 s). By 4.6 and 4.8 s, a large arc-shaped

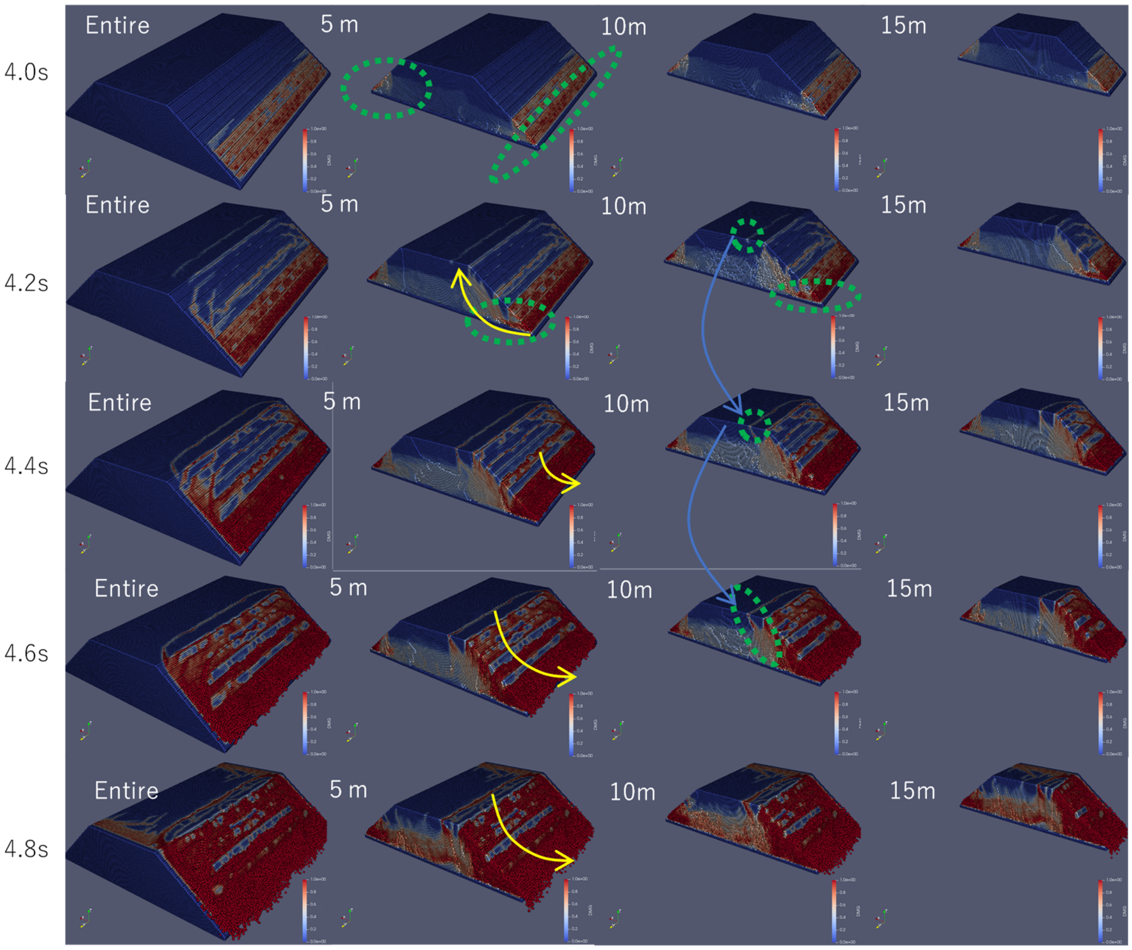

Fig. 5 Time-dependent damage distribution at each cross-section (Case (1): 320 Gal, 1 Hz)

sliding failure could be observed at the back side of the small arc-shaped damage region (yellow arrows at 5 m; 4.6 and 4.8 s). Thus, the failure could be characterized as sliding-type at 1 Hz. Additionally, the formation of arc-shaped damage regions at 4.2 and 4.4 s was accompanied by longitudinal cracks in the depth direction on the slope and crest. The arc shape was due to the 3D effects caused by the installation of walls on the front and back of the embankment. However, no significant variation in the failure mode was observed along the depth. Moreover, longitudinal cracks (damage zones) formed on the crest at 4.4 s. At 4.6 s, they connected with the arc-shaped damage zones that formed from the right side of the embankment (blue line and green circles at 10 m for 4.2, 4.4, and 4.6 s). This suggests that the crack progression at the crest might have combined with sliding cracks, leading to overall failure. Conversely, the left-side slope of the embankment showed only surface cracks up to 4.6 s, without reaching sliding failure during this time frame. Although the input seismic wave was symmetrical, asymmetrical failure occurred because once a crack initiated in a specific location, a new internal boundary was formed, altering the boundary conditions. Additionally, the energy released during crack propagation transmitted the acceleration from the crack tip, breaking the system's symmetry.

Unlike the 1 Hz results, in Fig. 6(a) at 2.3 s, Fig. 6(b) at 4.2 s, Fig. 6(c) at 3.7 s, and Fig. 6(d) at 3.1 s, open cracks (damage zones) began to form in the mid-slope area and progressed into the embankment over time (green circles in each figure). In Fig. 6(c) at 3.9 s, cracks progressed internally to the crest and slope (green circle and yellow arrow at 5 m), eventually causing collapse with the formation of small sliding soil blocks. Additionally, Fig. 6(a) at 2.7 s, Fig. 6(b) at 4.6 s, and Fig. 6(c) at 3.9 s show not only longitudinal cracks on the crest but also transverse cracks that were not reproducible in the 2D analysis. These trends were not observed in the 1 Hz case in Fig. 5, suggesting that higher frequency inputs could lead to transverse cracking at the crest. Initial open cracks also occurred at higher positions on the slope

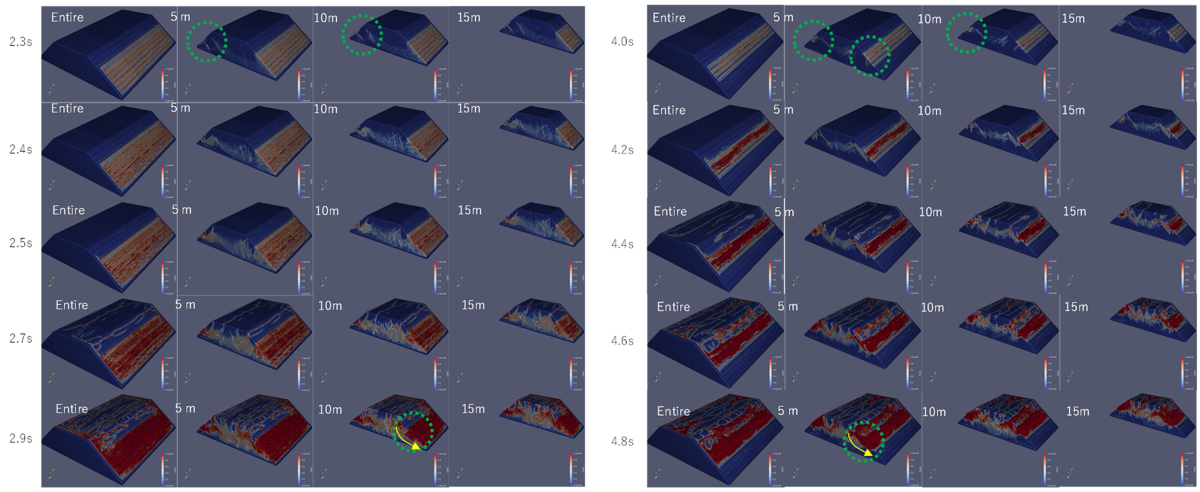

(a) 2 Hz (b) 3 Hz

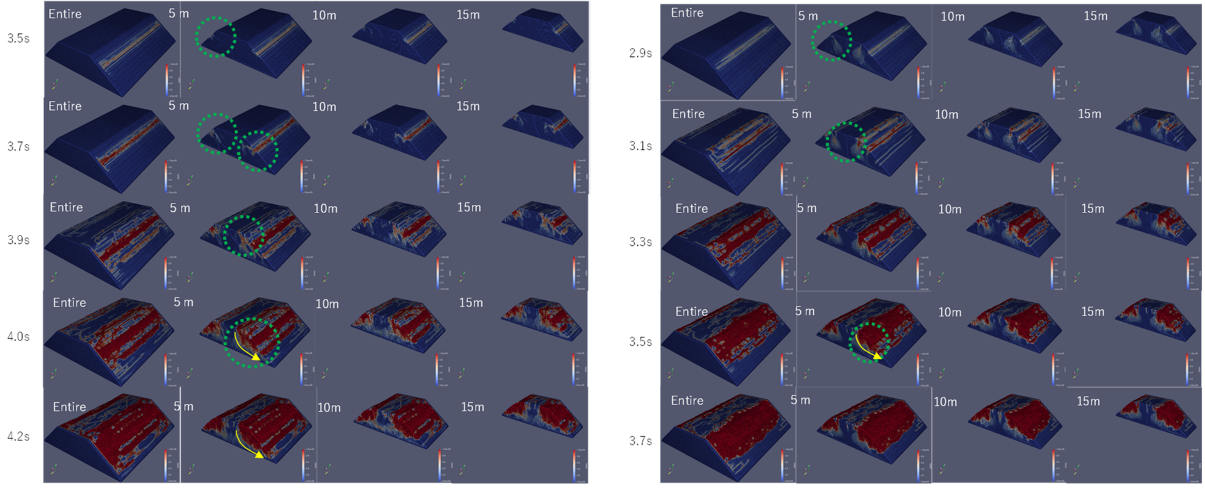

(c) 4 Hz (d) 5 Hz

Fig. 6 Time-dependent damage distribution at each cross-section (Case (1): 320 Gal, 2–5 Hz)

as the frequency increased—a trend consistent with the 2D analysis, as described in Section 3.1. Harada et al.5) concluded that differences in crack initiation positions are due to variations in the natural and input frequencies. The first natural frequency for this model, assuming a horizontally layered ground, was approximately 2.197 Hz, which was likely close to the actual first natural frequency of the model. Therefore, at 1 and 2–5 Hz, the phase shifted and the displacement amplitude peaked at 2 Hz and decreased at higher frequencies. This result was consistent with the failure that occurred the earliest at 2 Hz. The earlier failure progression at 5 Hz, compared with that at 4 Hz, suggests that the displacement amplitude may increase again as the frequency approaches the second natural mode. These results indicate that the deformation and failure modes change with the seismic wave frequency: low frequencies tend to induce sliding failure, whereas high frequencies induce open cracking early in the process. However, further research is needed to clarify the relationships among natural frequencies, mode shapes, crack initiation locations, and failure modes.

3.3 Analysis results for Case (2)

This section presents the results from Case (2), where the input frequency was set to 1 Hz and the peak ground acceleration was varied. Fig. 7 shows the results for the input accelerations ranging from 300 to 400 Gal. As shown in Figs. 7(a)–(c), where green circles and yellow arrows highlight the damage zones, lower acceleration values tend to cause damage at the slope toe, resulting in sliding failure.

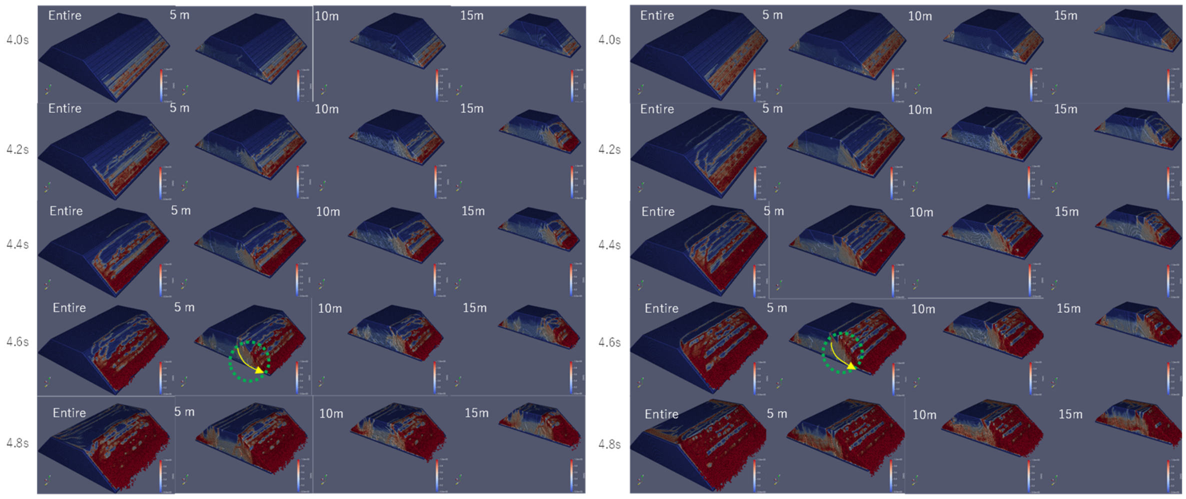

(a) 300 Gal (b) 320 Gal (reproduced)

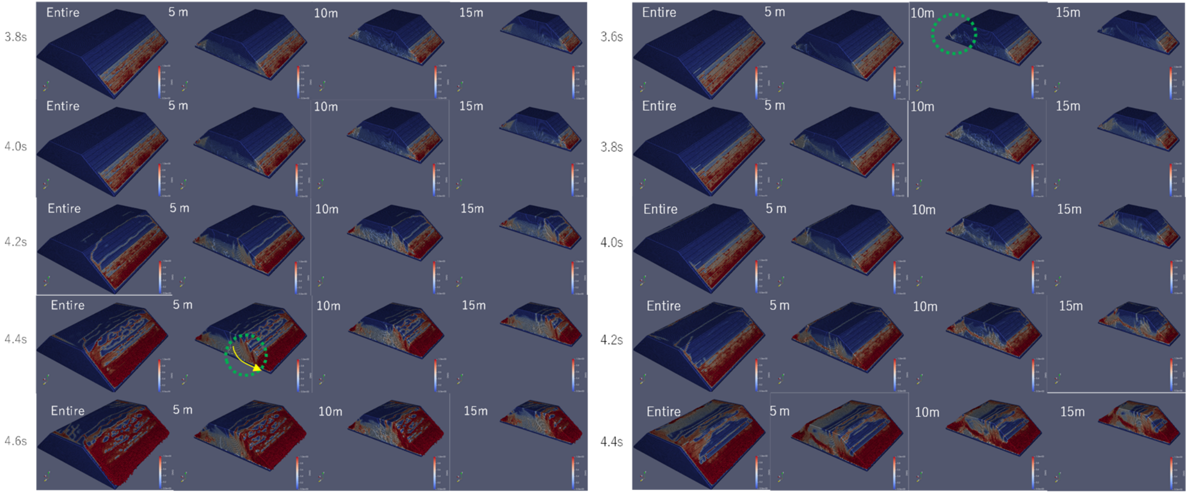

(c) 340 Gal (d) 360 Gal

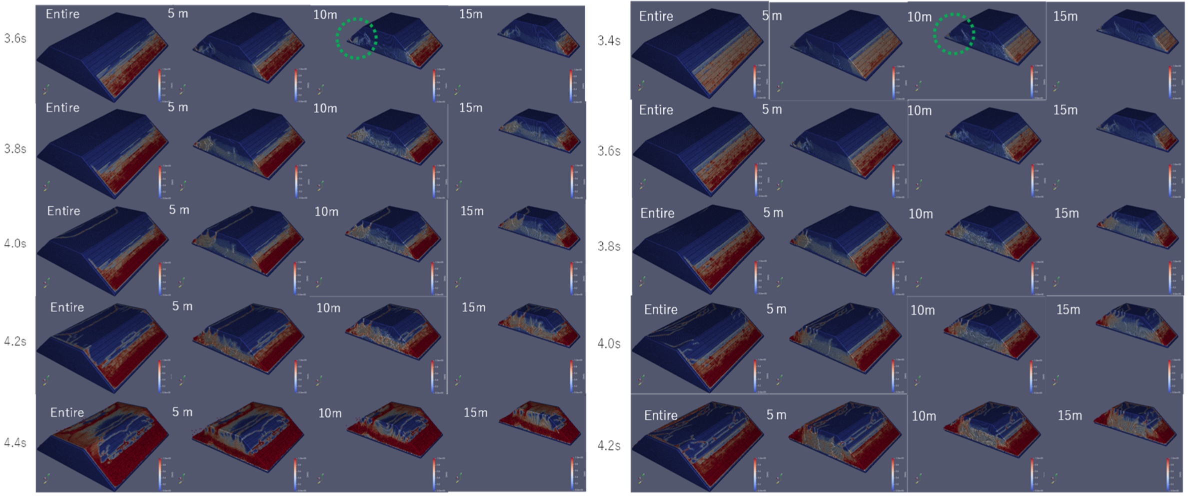

(e) 380 Gal (f) 400 Gal

Fig. 7 Time-dependent damage distribution at each cross-section (Case (2): 1 Hz, 300–400 Gal)

Conversely, at 360 Gal (Fig. 7(d), 10 m section at 3.6 s), a distinct damage zone formed at a low position on the rear (left side) slope. This trend was also apparent at 380 and 400 Gal. The 2D analysis also showed a similar tendency for failure to progress after crack formation on the slope when the peak acceleration was high. In this model, when the peak acceleration exceeded 360 Gal, the bottom of the embankment tended to experience widespread failure. This was likely due to the large amplitude caused by the high acceleration, which led to significant shear deformation and rupture at the embankment base as it displaced laterally.

4. CONCLUSION

In this study, we proposed a 3D PD analysis method for simulating crack propagation during seismic loading and applied it to a homogeneous embankment composed of compacted clay. The following conclusions were drawn:

1. Comparison with 2D analysis showed that the failure modes at the central cross-section of the 3D model qualitatively matched, demonstrating the validity of the proposed analysis code.
2. The 3D analysis revealed that low-frequency seismic inputs tended to induce sliding failure, whereas high-frequency inputs led to the formation of open cracks on the slope due to differences in the deformation mode. These cracks tended to initiate at higher positions as the frequency increased.
3. The 3D analysis also revealed longitudinal arc-shaped cracks in the depth direction and transverse cracks at the crest—features not captured in the 2D analysis.
4. When keeping the input frequency constant and varying the peak ground acceleration, no significant differences in the failure modes were observed for lower accelerations.

Future studies will be focused on clarifying the relationship between deformation and failure modes through eigenvalue analysis and on developing a quantitative evaluation method that accounts for both seismic-induced cracking and subsequent rainfall-induced sliding, considering groundwater levels.

ACKNOWLEDGMENT

This research was partially supported by the JSPS KAKENHI Grant-in-Aid for Scientific Research (C), Project Number 22K04307, the FY2023 “Joint Research Grant between National Institute of Technology and Nagaoka University of Technology,” and the FY2023 grant from the Soil Science Center Foundation. Part of the computations were conducted using the Fujitsu supercomputer PRIMEHPC FX1000 and the Fujitsu server PRIMERGY GX2570 (Wisteria/BDEC-01) at the Information Technology Center of the University of Tokyo. The authors express their sincere gratitude.

REFERENCES

1) Newmark, N. M.: Effects of Earthquakes on Dams and Embankments, *Geotechnique*, Vol. 15, No. 2, pp. 139–159, 1965.
2) Sato, H., Enomura, Y. and Yamaguchi, Y.: Cracking on Embankment Dams Due to Recent Large Earthquakes and Direct and Splitting Tensile Strength Tests for Core Material, *International Symposium on Bali*, Indonesia, 2014.
3) Harada, Y., Goto, H. and Sawada, S.: Initiation Process of Tension Cracks in Soil Embankment on Liquefied Sandy Ground Investigated from Centrifuge Model Test, *Soil Dynamics and Earthquake Engineering*, Vol. 161, 107444, 2022.
4) Wakinaka, K., Uzuoka, R., Matsuda, T. and Fujii, N.: Analysis of Damage Inside Embankment After Earthquake Based on Embankment Opening Survey, *Proceedings of the 58th Japanese Geotechnical Society Research Presentation*, 11-8-2-03, 2023 (in Japanese).
5) Harada, Y., Goto, H. and Sawada, S.: Study on Generation Mechanism of Open Cracks in the Soil Embankment Underlying Liquefiable Soil Ground, *Journal of Japan Society of Civil Engineers, Ser. A1 (Structural Engineering & Earthquake Engineering (SE/EE))*, Vol. 76, No. 4, pp. I_96–I_105, 2020 (in Japanese).

6) Ikeda, T., Goto, H. and Sawada, S.: Crack Propagation in Soil Embankment Based on X-FEM Considering Tensile Failure Mode, *Journal of Japan Society of Civil Engineers, Ser. A2 (Applied Mechanics (AM))*, Vol. 72, No. 2, pp. I_227–I235, 2016 (in Japanese).

7) Shimbo, T. and Yatomi, C.: On an Earthquake-Induced Separation Failure of a River Dike by a Crack Extension Analysis, *The Japanese Geotechnical Society Special Symposium—Overcome the Great East Japan Earthquake—*, Vol. 23, pp. 212–218, 2014 (in Japanese).

8) Kumamoto Prefecture: Tateno District Crack Measures Exploratory Committee Report, 2020 (in Japanese). https://www.pref.kumamoto.jp/soshiki/93/1875.html (last accessed on July 31, 2023)

9) Shimbo, T.: Development and Application of a Dynamic XFEM for the Seismic Residual Displacement Analysis of an Embankment, *Soils and Foundations*, Vol. 57, No. 3, pp. 357–370, 2017.

10) Shimbo, T., Itto, R., Inaba, K., Aaraki, K. and Watanabe, N.: Seismic Response Analysis for Ordinary State-Based Peridynamics in a Linear Isotropic Elastic Material, *Journal of Peridynamics and Nonlocal Modeling*, Vol. 2, pp. 185–204, 2020.

11) Itto, R., Kubo, H. and Shimbo, T.: Semi-Verification of Seismic-Response Analysis for an Embankment Using Peridynamics, *3rd International Conference on Computational Engineering and Science for Safety and Environmental Problems*, Kobe, Japan, 2020.

12) Shimbo, T., Adlan, M. K., Kawamura, T. and Fukumoto, Y.: Crack Propagation Analysis in an Embankment by Peridynamics focusing on Maximum Acceleration and Frequency of Input Seismic Wave, *Proceedings on 25th Applied mechanics symposium*, Online, Japan, pp. 2B01-06-02–2B01-6-02, 2022 (in Japanese).

13) Shimbo, T., Kawamura, T., Uchii, U. and Fukumoto, Y.: Crack Propagation Analysis in Embankments during Earthquakes Using Ordinary State-based Peridynamics, *15th World Congress on Computational Mechanics (WCCM-XV) 8th Asian Pacific Congress on Computational Mechanics (APCOM-VIII)*, Yokohama, Japan, 2022.

14) Shinzo, C., Shimbo, T. and Fukumoto, Y.: Crack Propagation Analysis of Compacted Clays with Various Water Contents Using Peridynamics, *The 7th International Conference on "Science of Technology Innovation" 2022*, p. 93, 2022.

15) Shimbo, T., Shinzo, C., Uchii, U., Itto, R. and Fukumoto, Y.: Effect of Water Contents and Initial Crack Lengths on Mechanical Properties and Failure Modes of Pre-Cracked Compacted Clay Under Uniaxial Compression, *Engineering Geology*, Vol. 301, 106593, 2022.

16) Fukumoto, Y. and Shimbo, T.: 3-D Coupled Peridynamics and Discrete Element Method for Fracture and Post-Fracture Behavior of Soil-Like Materials, *Computers and Geotechnics*, Vol. 158, 105372, 2023.

17) Silling, S. A.: Reformulation of Elasticity Theory for Discontinuities and Long-Range Forces, *Journal of the Mechanics and Physics of Solids*, Vol. 48, No. 1, pp. 175–209, 2000.

18) Madenci, E. and Oterkus, E.: *Peridynamic Theory and Its Applications*, 17th ed., Springer, Berlin, 289 pp., 2014.

19) Ma, X., Feng, Q., Liu, L., Xu, J., Zhang, P., and Chen, H.: A Non-Local Method in Peridynamic Theory for Simulating Elastic Wave Propagation in Solids, *Applied Mathematical Modelling*, Vol. 103, pp. 360–375, 2022.

20) Noda, S., Yashiro, K., Takahashi, K., Takemura, M., Ohno, S., Tohdo, M. and Watanabe, T.: Response Spectra for Design Purpose of Stiff Structures on Rock Sites, *Proceedings of the OECD-NEA Workshop on the Relation Between Seismological Data and Seismic Engineering Analysis*, Istanbul, pp. 399–408, 2003.

(Original Japanese Paper Published: March, 2025)
(English Version Submitted: June 2, 2025)
(English Version Accepted: July 18, 2025)